Polymorph separation induced by angle distortion and electron delocalization effect via orbital modification in VO_2 epitaxial thin films

Bin Hong,[1] Kai Hu,[1] Zhuchen Tao,[2] Jiangtao Zhao,[1] Nan Pan,[3] Xiaoping Wang,[3] Minghui Lu,[4] Yuanjun Yang,[1,2,*] Zhenlin Luo,[1,2,†] and Chen Gao[1,2,‡]

[1]*National Synchrotron Radiation Laboratory, Collaborative Innovation Center of Chemistry for Energy Materials, University of Science and Technology of China, Hefei, Anhui 230029, People's Republic of China*

[2]*CAS Key Laboratory of Materials for Energy Conversion, Department of Materials Science and Engineering, University of Science and Technology of China, Hefei, Anhui 230026, People's Republic of China*

[3]*Hefei National Laboratory for Physical Sciences at the Microscale, University of Science and Technology of China, Hefei, Anhui 230026, People's Republic of China*

[4]*Nanjing University, College of Engineering and Applied Science, Nanjing, Jiangsu 210093, People's Republic of China*

(Received 13 November 2016; revised manuscript received 3 February 2017; published 27 February 2017)

Since Morin discovered that vanadium dioxide (VO_2) undergoes a reversible and dramatic structural phase transition coupled with an abrupt metal-insulator transition, extensive attention has been paid to VO_2 due to its importance in fundamental condensed state physics and its potential technological applications. Here, we observed that the precipitated phases of VO_2 (insulating and metallic polymorphs) could be controlled by relaxing the dimerization of the vanadium-vanadium (V-V) atomic chain. In particular, the monoclinic metallic phase can be stabilized even at room temperature with the assistance of the angle-distortion-induced ($\beta = 120^\circ$) metallization through symmetry matching between the VO_2 epitaxial thin films and the (0001)-oriented sapphire substrates. Concomitantly, the insulating phase (M1, $\beta = 122.6^\circ$) that separates from the metallic matrix may supply another driving force for stabilizing the metallic phase, as indicated by scattering-type scanning near-field optical infrared microscopy and further confirmed by synchrotron radiation high-resolution x-ray diffraction characterizations. Soft x-ray absorption spectroscopy results showed that the orbital features of the monoclinic metallic phase are analogous to those of the high-temperature metallic rutile VO_2 (R) phase. First-principles calculations further demonstrate the angle-distortion-induced reduction of the V-V atomic dimerization, which enhances the electron delocalization and thus the conductivity. Therefore, the angle distortion results in the metallic monoclinic phase and stabilizes it with the assistance of the nanoscale insulating VO_2 (M1) domains at room temperature. These results are of great importance for understanding the contributions of various polymorphs to the metal-insulator transition and for the design of novel artificially heterointerfacial devices based on VO_2 nanoscale polymorphs.

DOI: 10.1103/PhysRevB.95.075433

I. INTRODUCTION

The prototypical electron-correlated insulator vanadium dioxide (VO_2) exhibits a reversible and abrupt metal-insulator transition (MIT) at approximately 341 K in the bulk coupled with a structural phase transition (SPT) from the high-temperature rutile VO_2 (R) phase to the low-temperature monoclinic VO_2 (M1) phase [1]. This material has been of broad interest for potential applications due to its sharp changes in infrared optical and resistive properties, which allow the use of VO_2 for infrared detectors [2], smart windows [3–5], field-effect transistors [6,7], memory devices [8,9], etc. On the other hand, the coupling mechanism of the structural and electronic transformations and their contributions to the metal-insulator transition are the basic problems in fundamental condensed matter physics [9–13]. To date, many experimental and theoretical studies have been conducted over the past 50 years to investigate these questions. Basically, two criteria have been claimed: a Peierls MIT driven by SPT through electron-lattice interactions and a Mott MIT driven by charge localization through electron-electron correlations [11,12,14–18]. However, the controversy has been continuing.

So far, numerous efforts have been directed at controlling the MIT behaviors (e.g., the critical temperature T_c of ~341 K in bulk VO_2). Some effective approaches for the manipulation of the MIT have been developed, such as the use of strain [19–23], optical fields [24,25], oxygen vacancies [26], doping [27,28], and electric fields [29–32]. However, the driving force and mechanism of the MIT under multifields are controversial and not well understood [32]. The abrupt MIT may be closely related to the formation of the V-V atom chains, corresponding to a change from a straight chain in the high-temperature metallic rutile phase to a zigzag chain with dimerized V atoms in the low-temperature insulating monoclinic phase [32–36]. Recently, many results also provided some conclusive evidence that a metastable anomalous metallic phase exists in the monoclinic VO_2 (M1) insulating phase [37–40]. The team of Siwick obtained metallic metastable states by the ultrafast photoinducing method in monoclinic VO_2 (M1) insulating phase [25]. Stähler *et al.* also demonstrated that the band gap of the insulating VO_2 (M1) collapses instantaneously to the delocalized states due to the photoexcitation of carriers from the localized vanadium 3*d* valence states, and their calculation results confirmed this physics picture as well [38]. Arcangeletti *et al.*

*yangyuanjun@ustc.edu.cn
†zlluo@ustc.edu.cn
‡cgao@ustc.edu.cn

found that the vanadium atoms rearrangement induces band gap collapses in the monoclinic VO_2 (M1) phase at room temperature but appears with the assistance of high pressure (>10 GPa) [41]. Bai *et al.* recently discussed the metallization mechanism based on the proposed crystal structure, and their results indicated that the metallization arises from several new phases (e.g., X phase VO_2, baddeleyite-like structure) under high pressure rather than from normal M1 phase VO_2 [40]. Therefore, understanding the metallization process and mechanism at room temperature within the insulating monoclinic phase VO_2 (M1) is very important for understanding the mechanism of the MIT. However, this question has been incompletely studied so far in the VO_2 system. Furthermore, due to the recent advances in the deposition techniques and the large demands placed on thin-film devices based on VO_2, a considerable amount of work has focused on the VO_2 epitaxial thin films with superior crystal quality [42,43]. Meanwhile, for the VO_2 epitaxial thin films, the roles of the strain and nanoscale morphology of VO_2 thin films become prominent, dramatically affecting the behaviors and even the distinct mechanisms of the MIT [21,44–46]. Herein, we experimentally observed the angle-distortion-induced polymorph separations and metallization ($\beta = 120^\circ$) in the abnormal mixed-phase VO_2 epitaxial thin films without the assistance of high pressures or an ultrafast laser. Importantly, the metallic state can be stabilized at room temperature. Moreover, the insulating monoclinic phase (M1, $\beta = 122.6^\circ$) separates from the metallic monoclinic phase ($\beta = 120^\circ$). Synchrotron radiation x-ray absorption spectroscopy (XAS), x-ray diffraction (XRD), and first-principles calculations further demonstrated that the angle distortion reduces the V-V atomic dimerization, enhancing the electron delocalization behavior. In addition, the orbital features of the mixed-phase VO_2 thin films are analogous to those of the high-temperature metallic rutile VO_2 (R) crystalline structure.

II. RESULTS AND DISCUSSION

In this work, through the optimization of the deposition conditions (see experimental and theoretical methods), abnormal VO_2 epitaxial thin films with the angle distortions were obtained due to the symmetry mismatch between monoclinic VO_2 thin film and hexagonal sapphire substrate and also the growth process (grown at high temperature and then cooling down to room temperature). The film thickness of approximately 120 nm was measured using x-ray reflectivity (see Supplemental Material, Fig. S1 [47]). The electrical transport properties were measured for the normal VO_2 (M1 phase) and abnormal VO_2 thin films as shown in Figs. 1(a) and 1(b). The temperature-dependent resistivity of VO_2 (M1) is in good agreement with the literature results [21], also demonstrating the MIT critical temperature of ∼339 K. However, for the abnormal VO_2 thin films, the resistivity vs temperature curve exhibits metallic characteristics with lower resistivity ($\sim 10^{-2}$ to $10^{-3}\,\Omega\,\mathrm{cm}$) than that of the normal M1 VO_2 thin films ($\sim 10^{2}$ to $10^{-2}\,\Omega\,\mathrm{cm}$) in the relevant temperature range. More interestingly, there is still a subtle phase transition [as shown in the inset of Fig. 1(a)]. We further checked that this subtle phase transition in the ensemble measurements originate from M1-phase islands by temperature-dependent scanning near-field microwave microscopy measurements (see Supplemental Material, Fig. S2). The corresponding critical temperatures are $T_{\mathrm{heating}} \sim 351$ K and $T_{\mathrm{cooling}} \sim 341$ K during the heating and cooling cycles, as obtained from the differential resistivity-temperature curves in Fig. 1(b).

To investigate the aforementioned abnormal behaviors of the MIT, the surface morphology was first characterized. A large amount of self-organized domain patterns separate out from the matrix of the VO_2 thin films, as observed by atomic force microscope (AFM) characterization and shown in Fig. 1(c). The domains are randomly distributed. The magnified image in Fig. 1(d) quantitatively showed that the domains are uniform with a diameter of ∼200 nm and height of ∼127 nm. Furthermore, previous experimental investigations in recent years have revealed that many transition-metal oxides are inhomogeneous at the nanoscale and even microscale, and the inhomogeneity directly influences their properties such as MIT and colossal magnetoresistance [44,45,48,49]. For example, Qazilbash *et al.* directly observed the coexistence of insulating and metallic phases in VO_2 thin films over a critical temperature range in the transition region via scattering-type scanning near-field optical infrared microscopy (s-SNOIM) nanoimaging. They demonstrated that metallic islands nucleate at grain boundaries, where the variations in electronic structure and strain distribution obviously affect the MIT behaviors [48]. Therefore, it is conjectured that the nanoscale domains and matrix may have distinct electrical properties leading to the abnormal MIT behaviors above.

To distinguish between the separated phases of the nanoscale domain and the matrix, the s-SNOIM technique was used (see experimental and theoretical methods). The s-SNOIM setup is schematically shown in Fig. 1(e). Figure 1(f) shows the near-field scattering amplitude image obtained at an infrared wavelength $\lambda \sim 10.2\ \mu$m. At this midinfrared wavelength, the optical conductivity contrast of the insulating and metallic phases of VO_2 is large enough to distinguish the near-field amplitude signal [48]. The near-field signal S_3 was extracted from the data presented in Fig. 1(f) as the near-field scattering amplitude using the pseudoheterodyne detection scheme with third-harmonic demodulation. The signal of the scattering amplitudes from the matrix of the VO_2 thin films is much higher than that of the nanoscale domains. Combining the large difference in the scattering amplitudes between the nanoscale domain and the matrix and the previous reports [37,45,48,50,51], we can safely distinguish between the insulating and metallic regions in these VO_2 thin films. The nanoscale domains should be insulating (M1 phase), but the matrix should be metallic and is labeled as the mM phase in Fig. 1(f). Therefore, this kind of VO_2 thin film is a mixed-phase system with two possible different electronic phases (mM and M1 VO_2). The volume ratio of the M1 and mM phases is derived to be ∼1/3 from the above AFM characterizations [see Supplemental Material, Fig. S3(a)]. More interestingly, the *I-V* curves at the different localized zones in the mixed-phase VO_2 thin films show different rectifier characteristics (see Supplemental Material, Fig. S4), further indicating that the matrix is metallic, but nanoscale domains are insulating.

It is well known that the MIT is often accompanied by a SPT [52–54]. To study the role of the SPT in the MIT, the structural characterizations of the abnormal VO_2

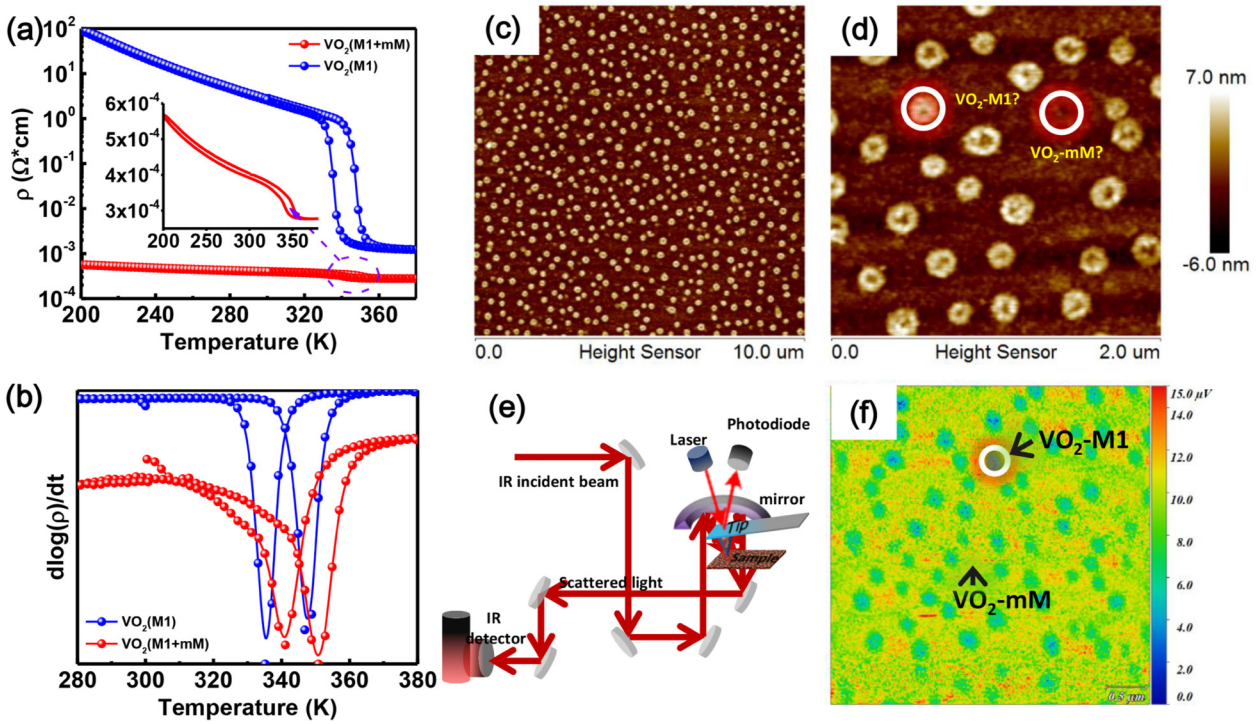

FIG. 1. Resistivity vs temperature curves and microscopic images of VO_2 thin films. (a) Temperature-dependent resistivities ρ for normal VO_2 (M1) and abnormal VO_2 thin films. (b) Derivative of the logarithmic electrical resistivity curves and the temperature derivative of $\log(\rho)$. AFM topographical images of the abnormal VO_2 thin films in (c) with scan range 10 μm × 10 μm and (d) zoomed scan range 2 μm × 2 μm. Schematic illustration of the s-SNOIM setup (e) and optical amplitude S_3 image of s-SNOIM for the angle distortion of VO_2 films showing pure near-field response. The scan range is 4 μm × 4 μm in size and obtained at the infrared wavelength $\lambda = 10.2\,\mu$m. The metallic phase is in the light (yellow, red) colors and the insulating phase is in the dark (cyan, blue) colors.

thin films were performed using synchrotron radiation high-resolution XRD with varying *in situ* temperature across the MIT to examine precise lattice structure transformations and the subtle transition behaviors. Figure 2(a) shows the temperature-dependent synchrotron radiation XRD patterns of the abnormal VO_2 thin films at the incident wavelength $\lambda = 1.2398$ Å. The sharp peaks around ~33.28° and 31.89° are assigned to the (0001) plane of the sapphire substrate and the (020) plane of VO_2 (M1), respectively. Moreover, a small peak is observed near the (020) peak of the M1 VO_2 phase in Fig. 2(a). This peak at ~31.68° should correspond to the (020) plane of the metallic matrix of the VO_2 thin films, referred to as the VO_2 (mM) phase. After fitting XRD experimental data, the volume ratio of M1 and mM phases in the sample is ~1/3, which is in good agreement with the AFM [see Supplemental Material, Fig. S3(b) and Table S1]. Moreover, unlike the normal VO_2 thin films with the pure M1 phase, both the (020) peaks of VO_2 (M1) and VO_2 (mM) phases do not shift with increasing temperature, indicating the absence of the monoclinic to rutile phase transition (see Supplemental Material, Fig. S5) [55]. On the one hand, this behavior may be ascribed to the clamping effect via the symmetry mismatch between the mM VO_2 thin films and hexagonal sapphire substrates. On the other hand, the M1 VO_2 polymorphs embed in the mM matrix and serve as the strain-mediation center. Thus, the heterointerfacial strain between the mM and M1 VO_2 polymorphs may lock the crystal structure across the MIT and probably suppress the structural phase transition. Consequently, the obvious structural phase transition expected in the pure M1 VO_2 thin films was not observed in the mixed-phase VO_2 thin films studied here. This subtle phase transition should be closely related to the electronic transition as reported previously and not accompanied by structural phase transition [56,57].

To exclude the possible influences of the impurity phases and different valence states, we performed high-resolution x-ray photoelectron spectroscopy measurements of the mixed-phase VO_2 thin films. Figure 2(b) presents the experimental and fitting results of the V 2p and O 1s peaks. The $V^{4+}2p_{3/2}$ and $V^{4+}2p_{1/2}$ are located at the binding energies of 516.1 and 523.46 eV, respectively. The O 1s binding energy is approximately 530.1 eV. These results are in good agreement with the previous results [58,59]. An additional O 1s peak is located at ~531.68 eV and is consistent with the O-H bonding. Herein, it is believed that there is no indication of any other V valence states except for V^{4+} that is ascribed to impurity phases. Therefore, the metallization of mM VO_2 and the origin of the subtle transition are not related to the valence states and impurity phases, but should be due to the intrinsic effect of the mixed-phase VO_2 thin films.

In order to further study the essence of the separated electronic phases, Raman spectra were measured to investigate phonon behaviors or lattice vibrations with the Raman active modes at the Γ point of the Brillouin zone. Figures 2(c) and 2(d) present the evolution of the Raman spectra with varying *in situ* temperature for the pure VO_2 (M1) and mixed-phase VO_2

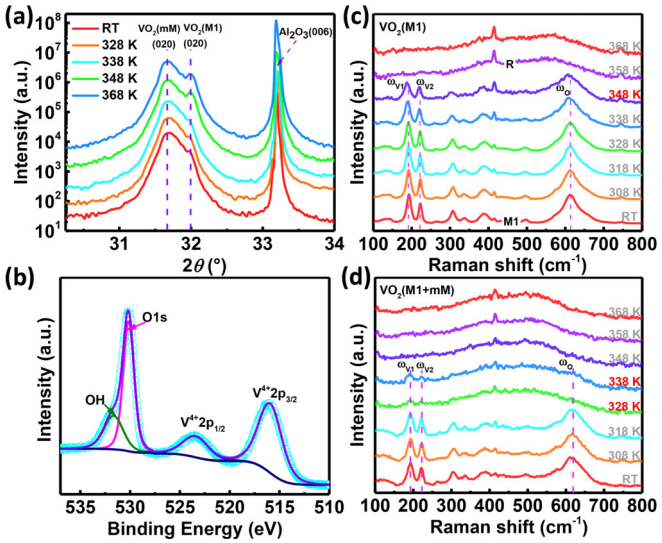

FIG. 2. (a) θ-2θ scans of the synchrotron radiation XRD curves of the mixed-phase VO_2 thin films at various *in situ* temperatures. (b) High-resolution XPS measurements. V $2p$ core-level spectra (dotted line) and corresponding fitting results (solid lines). (c) Temperature dependence of the Raman spectra for the VO_2 (M1) thin films (c) and of the mixed-phase VO_2 thin films (d). Dashed lines mark the phonon peaks ω_{V1},ω_{V2}, and ω_O.

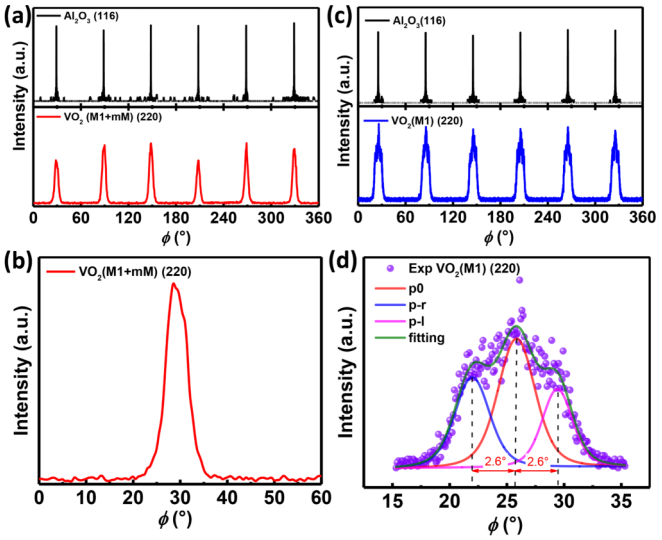

FIG. 3. XRD phi scans of VO_2 on Al_2O_3 (0001) substrates. Full phi scans of the (220) planes of the mixed-phase VO_2 thin films (a) and VO_2 (M1) thin films (b) with respect to the (116) planes of the substrates. Magnified image of the XRD phi scans of the VO_2 (mM+M1) thin films in (c), and VO_2 (M1) that quantitatively indicated that each of the main peaks (labeled p0) has two satellite peaks (labeled p-l and p-r) at approximately 2.6°.

(mM+M1) thin films, respectively. The representative Raman spectrum of the VO_2 exhibits three prominent vibration modes at ∼193, 222, and 616 cm^{-1} [dashed lines mark the phonon peaks as shown in Figs. 2(c) and 2(d)] at room temperature, denoted as low-frequency ω_{V1},ω_{V2}, and high-frequency ω_O, respectively (see Supplemental Material, Fig. S6). The low-frequency Raman peaks ω_{V1} and ω_{V2} are ascribed to the V-V atom vibrations, whereas the phonon frequency ω_O is directly related to the V-O atom vibrations [60,61]. Specifically, the disappearance of the high-frequency ω_O between $T =$ 328 K and $T =$ 338 K [Fig. 2(d)] for the mixed-phase VO_2 (M1+mM) thin films indicates that the V-O lattice motion modes are analogous to the metallic rutile VO_2 (R) crystalline structure. Moreover, the low-frequency Raman shifts of the ω_{V1} and ω_{V2} modes still exist at higher temperature between 328 and 338 K but disappear in the case of the pure M1 VO_2 thin films. Then, the three typical peaks all disappear at high temperature. Hence, the rearrangements of the V-V atom chains should occur, but they do not change the macroscopic crystal structures and thus there is no SPT observed here.

For revealing the structural origin of the abnormal metallic phases at room temperature, high-resolution XRD phi scans were carried out to investigate the epitaxial relationships between the VO_2 thin films and sapphire substrates, and the domain configurations were also derived. The typical phi scans of the (220) peaks of the VO_2 thin films with different polymorphs on the (0001) planes of the sapphire substrates are plotted in Figs. 3(a) and 3(b). As shown in Fig. 3(a), the six peaks of the mixed-phase VO_2 (220) planes exhibit sixfold symmetry instead of the expected twofold symmetry in the framework of the monoclinic symmetry. Actually, the six peaks should arise from the three equivalent a axes of the mixed-phase VO_2 thin films, matching the (0001) surface plane of the sapphire substrate with the hexagonal symmetry. The schematic drawings of epitaxial matching relations between the mixed-phase VO_2 thin films and sapphire are shown in Fig. 4(a) ($\beta = 120°$). In the case of the normal pure M1 phase VO_2, the six main peaks of (220) planes [labeled p0, as shown in Figs. 3(c) and 3(d)] exhibit sixfold symmetry, and each of the main peaks has two satellite peaks (labeled p-l and p-r) at approximately $\pm 2.6°$. In fact, this feature is due to the angle mismatch between the β angle (122.6°) of VO_2

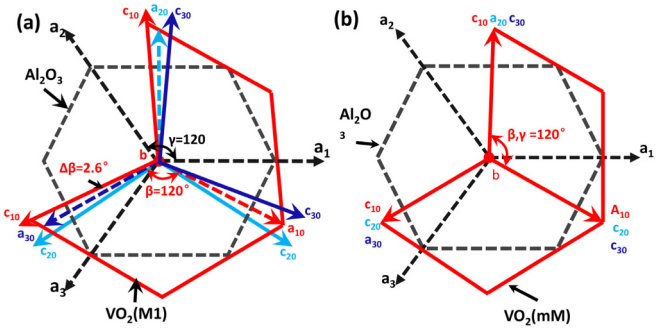

FIG. 4. Schematic drawings of the epitaxial matching relations between the angle distortions of the VO_2 thin films (mM or M1) and sapphire substrates at the interface. Lattices a (a_{10}, a_{20}, and a_{30}) or c (c_{10}, c_{20}, and c_{30}) only have three possible orientations because of the symmetry matching relationship on the (0001)-oriented sapphire substrate ($\beta = \gamma$) in (a). The β angle is reduced from the relaxed states (∼122.6°) of the VO_2 (M1) thin film to the angle of 120°. The β angle is thus compressed along the in-plane direction. For the VO_2 (M1) films, both lattices a and c have three possible orientations due to the symmetry mismatching (β∼122.6°) as shown in (b). This case is very common in the M1 VO_2 thin films on the sapphire substrates [62,63].

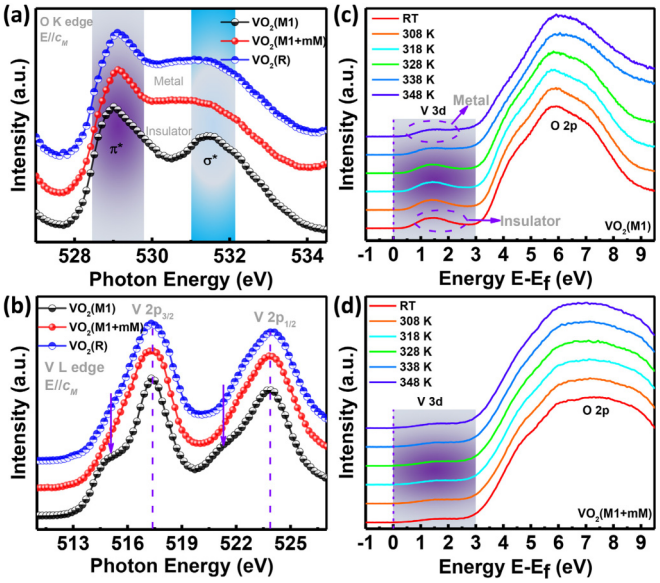

FIG. 5. High-resolution synchrotron radiation XAS and UPS results for the M1 VO_2 and mixed-phase VO_2 thin films. (a) O K-edge spectra from the O $1s$ level to the π^* and σ^* orbitals. (b) V L-edge transitions from $2p$ to $3d$ orbitals. The spectra are normalized to the maximum intensity and displaced vertically for clarity. UPS measurements of VO_2 (M1) (c) and the mixed-phase VO_2 thin films (d) across the MIT recorded on the same part.

(M1) and the γ (120°) angle of the sapphire substrates, as has been observed experimentally in the pure M1 phases [62,63]. Corresponding schematic drawings of the epitaxial relations between the VO_2 (M1) and sapphire substrate are illustrated in Fig. 4(b). Comparing these two cases, the angle β of the mixed-phase VO_2 thin films is decreased and thus is reduced from the relaxed states (∼122.6° of the pure M1 VO_2 thin films) to the angle of 120°. Therefore, this angle mismatching with the sapphire substrate results in the drastic modification of the V-V atom chains [454]. The overall effect is that the in-plane unit cell is expanded, and thus the shrinkage of the lattice constant b is observed, as shown in Fig. 2(a). Consequently, the V-V distance is enlarged along the atom chain, enhancing the electron delocalization. The metallization appears accessibly via the angle distortion ($\beta = 120°$) in the mixed-phase VO_2 thin films, and the metallic phase is thus stabilized at room temperature, with the nanoscale VO_2 M1 polymorphs serving as the strain accommodation centers.

In order to reveal the metallization of the mixed-phase VO_2 thin films at room temperature via the angle distortion, the orbital redistribution of the V atoms was investigated by soft x-ray spectroscopic techniques. We presented the synchrotron radiation XAS studies on the VO_2 thin films at the O K-edge and V L-edge absorption at room temperature. The various hybridized valence states can be distinguished from the XAS data that allow separate studies of the hybridized V $3d$ and O $2p$ orbitals near the Fermi level. As shown in Fig. 5(a), the spectra of all the different VO_2 polymorphs consist of a prominent doublet corresponding to the transitions from the O $1s$ level to the π^* and σ^* orbitals [64]. Among these, the O $1s$ orbital features of the mixed-phase VO_2 thin films resemble to a large extent those of the metallic rutile VO_2 (R) phases but are unlike those of the pure M1 VO_2 thin films. Most importantly, the V L edge contains the signatures of two pronounced maxima at 517.5 and 523.8 eV, roughly corresponding to the electron excitations from the respective spin doublet $2p_{3/2}$ and spin singlet $2p_{1/2}$ levels. However, the two shoulders near the main peaks in the pure M1 VO_2 thin films both disappear in the R and mixed-phase (mM+M1) VO_2 thin films. Based on this analysis of the spectra, we conclude that the angle distortion in the mixed-phase VO_2 thin films results in the distinct differences in the features of the V atom orbitals with respect to the pure M1 phase. However, the orbital features of the mixed-phase VO_2 thin films are very similar to those of the R phase (see Supplemental Material, the XRD of the pure rutile phase in Fig. S7). Therefore, we can boldly state that the orbital modifications through the angle-distortion-induced V-V atom chains may stabilize the novel monoclinic phase (mM) with room-temperature metallicity and allow the MIT even without the assistance of the SPT.

To further study the similarities of the electronic structure of this novel phase to the metallic rutile phase, we now turn to the temperature-dependent ultraviolet photoelectron spectroscopy (UPS) to directly explore the changes in electron occupancy behaviors near the Fermi energy E_f of the V $3d$ orbitals as shown in Figs. 5(c) and 5(d). The similarity in the electronic structure between the high-temperature rutile phase and the mixed-phase VO_2 thin films is easy to see: the UPS of the metallic phase [$T > T_c$, UPS as shown in Fig. 5(c) when temperature $T = 338$ K] of the VO_2 (M1) and the mixed-phase VO_2 [in Fig. 5(d)] thin films both have plateaus [37,38] that are the same as the metallic Fermi level features. However, the VO_2 (M1) phase still shows obvious insulating behavior [37] from the Fermi level at lower temperatures (T<338 K), as indicated by the shaded area in Fig. 5(c). These results are also in good agreement with those obtained by the s-SNOIM, high-resolution XRD and XAS studies described above. Therefore, at room temperature, the electronic structure of the VO_2 thin film with angle distortion is analogous to that of the VO_2 rutile phase with metallicity ($T > T_c$). It is mentionable that the UPS spectra were calibrated using the Fermi level of Au such that the Fermi level is located at 0 eV (see Supplemental Material for more measurement details, Fig. S8). The angle distortion may reduce the V-V atomic dimerization by expanding the lattice, indicating that the electrons may be delocalized at room temperature. Therefore, the novel monoclinic metallic mM phase is observed in the mixed-phase VO_2 thin films and is stabilized even at room temperature.

In addition to demonstrating the angle-distortion-induced metallicity in these novel VO_2 thin films and improving the understanding of the effects of the electron delocalization behaviors, *ab initio* calculations were performed with the Cambridge serial total energy package (CASTEP) software, and density functional theory (DFT+U) was used to study the electronic structures of the novel VO_2 (mM) thin films with the angle distortion. We first relaxed the atomic structure as shown in Figs. 6(a) and 6(b). In the monoclinic M1 structure, the angle β is 122.6°, and dimerization of the V-V atom chains is observed with V-V separations of 2.48 and 3.31 Å along the c_R axis (in tetragonal notation or the a_{M1} axis in monoclinic notation) as shown in Fig. 6(a). The band gap is found to be 0.6 eV for the M1 phase structure

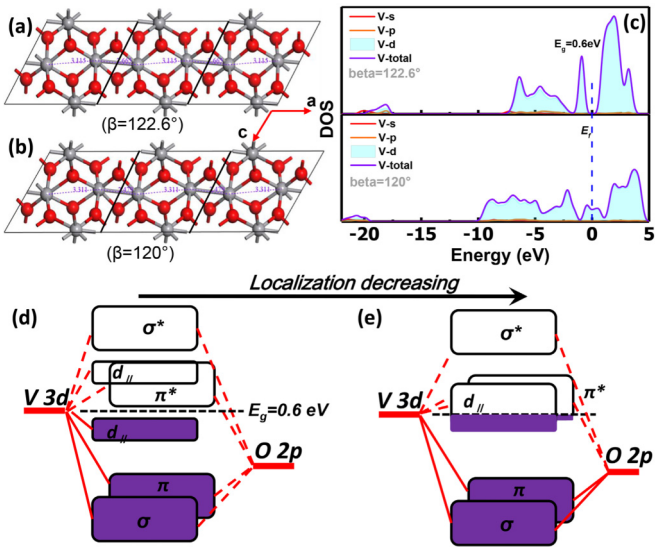

FIG. 6. Schematic of the VO_2 crystal structure projected into the monoclinic b axis and the rearrangement of the V-V chains: (a) $\beta = 122.6°$, V-V separations of 2.66 and 3.11 Å and (b) $\beta = 120°$, V-V separations of 2.48 and 3.31 Å. (c) The results of first-principles calculations. Schematic electronic structure of VO_2 according to Goodenough [67] in the insulating (d) and metallic (e) forms.

[shown in Fig. 6(c)], in good agreement with the literature values [54].

However, in the monoclinic mM structure of the angle-distorted VO_2, the β angle is set to 120°, and then, the lattice is relaxed to the stable state via the DFT calculations. A rearrangement of the V-V chains relative to the M1 phase shown in Fig. 6(a) is observed, and the V-V separations are changed to 2.66 and 3.11 Å, as shown in Fig. 6(b). The DFT calculations show that larger V-V distances imply hardly any d-orbital overlap (see the band structure of the VO_2 M1 phase in Fig. 6(c)). Moreover, the rearrangement of the V-V atom chains drastically modulates the band structure of the VO_2 mM phase. The V 3d electron has been delocalized and occupies the Fermi level as shown in Fig. 6(c), leading to the enhanced conductivity in the mixed-phase VO_2 (mM+M1) thin films. As shown in Fig. 6(d), the band gap of the insulating phase collapses instantaneously upon electron delocalization due to the expanding V-V distances [a schematic diagram of the electronic structure according to Goodenough [65] is shown for the metallic state in Fig. 6(e)]. Therefore, our calculations allow us to conclude that the occurrence of the metallicity that is stabilized at room temperature and observed experimentally in these novel VO_2 thin films is mainly ascribed to the electronic structure changes that are likely due to the V-V atom chain rearrangement via the angle distortion.

III. CONCLUSION

To summarize, we have controllably fabricated the novel mixed-phase VO_2 thin films on sapphire by reactive sputtering deposition. The AFM and s-SNOIM reveal that the insulating VO_2 (M1) domains are inlaid in the metallic mixed-phase VO_2 matrix. The observed inhomogeneous mixed phases can dramatically decrease the resistivity of the VO_2 thin films. Microscopy techniques also confirmed that the matrix is metallic, whereas the separated nanoscale domains (diameter of ~200 nm and height of ~7 nm) are insulating. The synchrotron radiation characterizations (XRD, XAS, and UPS) also further demonstrated that the metallic matrix is monoclinic and exhibits an electronic structure that is similar to that of the rutile metallic phase. Nevertheless, the nanoscale domains should be the M1 phase ($\beta = 122.6°$). Thus, the abnormal metallic mM phase VO_2 that is stabilized at room temperature results from the polymorph separation via the angle distortion and electron delocalization by orbital modification. Consequently, the mixed-phase VO_2 thin films show distinctive MIT behaviors comparing to the normal M1 phase. The structural phase transition is absent here, whereas the electronic transformation is responsible for the subtle MIT. Studies on the *in situ* characterization of the film growth and polymorph separation are needed and will be performed in the future. Our observations are of great importance in understanding the fundamental MIT as well as the metallization induced by the angle-distortion-driven delocalization process in these novel monoclinic VO_2 epitaxial thin films and provide a new route for controlling the electrical properties of VO_2 thin films through the tuning of the angle distortion.

IV. EXPERIMENTAL AND THEORETICAL METHODS

Through precise control of the vanadium arrival rate (sputtering power) and the oxidation of vanadium, a series of high-quality VO_2 single crystalline thin films (B, M, and R polymorphs) were epitaxially grown on (0001)-oriented sapphire substrates by reactive sputtering deposition; the details of the fabrication process are as described in our previous report [57].

For the s-SNOIM, we note that the complex conductivity $\tilde{\sigma}(\omega)$ of materials is generally related to their dielectric constant [44,48]:

$$\tilde{\varepsilon}(\omega) = 1 + \frac{4\pi i}{\omega}\tilde{\sigma}(\omega). \tag{1}$$

The near-field signal is generated with incident infrared radiation between the AFM tip and the sample. In this extended dipole model, the polarized AFM tip is modeled as a spherical dipole to describe the near-field interaction of the tip with the sample. By solving this tip-sample system of electrostatic equations, the effective polarizability of the coupling system is described as [47,66,67]

$$\alpha_{\text{eff}} = \frac{\alpha(1+\beta)}{1 - \frac{\alpha\beta}{16\pi(a+z)^3}}, \tag{2}$$

where α is the polarizability of the AFM tip, β is the surface response function of the sample, a is the radius of the tip sphere, and z is the tip-sample distance. Consequently, the near-field interaction is experimentally accessible via the measurement of the scattered intensity $E_s \propto |\alpha_{\text{eff}}|^2$.

First-principles calculations are performed using the CASTEP code with the generalized gradient approximation. The exchange-correlation functional of Perdew, Burke, and Ernzerhof is chosen. Ultrasoft pseudopotentials were used for all atomic species, and the plane wave basis cutoff energy is

set to 750 eV. A ($3 \times 3 \times 3$) Monkhorst-Pack grid is used for the relaxation of the supercells, and all structures were fully relaxed with the force tolerance of 0.01 eV/Å.

ACKNOWLEDGMENTS

This work was partially supported by the National Key Research and Development Program of China (Grant No. 2016YFA0300102). This work was also supported by the National Natural Science Foundation of China (Grant No. 51402281 and No. 11374010) and Anhui Natural Science Foundation (Grant No. 1508085QA06). We gratefully acknowledge Xingmin Zhang, Yueliang Gu, Lijuan Zhang, Renzhong Tai, and Xingyu Gao for the structural characterizations at beamline BL14B and BL08U1A of Shanghai Synchrotron Radiation facility (SSRF). We also thank Huanxin Ju, Qian Xu, Junfa Zhu, and Wensheng Yan for the spectrum measurements at the photoelectron spectroscopy endstation and magnetic circular dichroism endstation of National Synchrotron Radiation Laboratory (NSRL). This work was partially carried out at the USTC Center for Micro and Nanoscale Research and Fabrication, and we also thank Jinlan Peng, Xiaolei Wen, and Linjun Wang for their help on the AFM and s-SNOIM measurements.

[1] F. J. Morin, Phys. Rev. Lett. **3**, 34 (1959).
[2] S. H. Chen, H. Ma, X. J. Yi, T. Xiong, H. C. Wang, and C. J. Ke, Sens Actuators, **115**, 28 (2004).
[3] H. Kim *et al.*, ASC Nano **7**, 5769 (2013).
[4] C. Batista, R. M. Ribeiro, and V. Teixeira, Nanoscale Res. Lett. **6**, 301 (2011).
[5] J. Zhou, Y. Gao, Z. Zhang, H. Luo, C. Cao, Z. Chen, L. Dai, and X. Liu, Sci. Rep. **3**, 3029 (2013).
[6] Z. Yang, C. Ko, and S. Ramanathan, Annu. Rev. Mater. Res. **41**, 337 (2011).
[7] N. Shukla, A. V. Thathachary, A. Agrawal, H. Paik, A. Aziz, D. G. Schlom, S. K. Gupta, R. Engel-Herbert, and S. Datta, Nat. Commun. **6**, 7812 (2015).
[8] T. Driscoll *et al.*, Science **325**, 1518 (2009).
[9] L. Pellegrino, N. Manca, T. Kanki, H. Tanaka, M. Biasotti, E. Bellingeri, A. S. Siri, and D. Marre, Adv. Mater. **24**, 2929 (2012).
[10] S. Kumar, J. P. Strachan, M. D. Pickett, A. Bratkovsky, Y. Nishi, and R. S. Williams, Adv. Mater. **26**, 7505 (2014).
[11] Z. Tao, T.-R. T. Han, S. D. Mahanti, P. M. Duxbury, F. Yuan, C.-Y. Ruan, K. Wang, and J. Wu, Phys. Rev. Lett. **109**, 166406 (2012).
[12] S. Biermann, A. Poteryaev, A. I. Lichtenstein, and A. Georges, Phys. Rev. Lett. **94**, 026404 (2005).
[13] T. Yao, X. Zhang, Z. Sun, S. Liu, Y. Huang, Y. Xie, C. Wu, X. Yuan, W. Zhang, Z. Wu, G. Pan, F. Hu, L. Wu, Q. Liu, and S. Wei, Phys. Rev. Lett. **105**, 226405 (2010).
[14] P. Baum, D.-S. Yang, and A. H. Zewail, Science **318**, 788 (2007).
[15] H. Zheng and L. K. Wagner, Phys. Rev. Lett. **114**, 176401 (2015).
[16] J. H. Park, J. M. Coy, T. S. Kasirga, C. Huang, Z. Fei, S. Hunter, and D. H. Cobden, Nature (London) **500**, 431 (2013).
[17] P. Limelette, A. Georges, D. Jérome, P. Wzietek, P. Metcalf, and J. M. Honig, Science **302**, 89 (2003).
[18] R. M. Wentzcovitch, W. W. Schulz, and P. B. Allen, Phys. Rev. Lett. **72**, 3389 (1994).
[19] B. Hu, Y. Ding, W. Chen, D. Kulkarni, Y. Shen, V. V. Tsukruk, and Z. L. Wang, Adv. Mater. **22**, 5134 (2010).
[20] B. Hu, Y. Zhang, W. Chen, C. Xu, and Z. L. Wang, Adv. Mater. **23**, 3536 (2011).
[21] L. L. Fan *et al.*, Nano Lett. **14**, 4036 (2014).
[22] J. Cao *et al.*, Nat. Nanotechnol. **4**, 732 (2009).
[23] N. B. Aetukuri *et al.*, Nat. Phys. **9**, 661 (2013).
[24] W.-P. Hsieh, M. Trigo, D. A. Reis, G. Andrea Artioli, L. Malavasi, and W. L. Mao, App. Phys. Lett. **104**, 021917 (2014).
[25] V. R. Morrison, R. P. Chatelain, K. L. Tiwari, A. Hendaoui, A. Bruhacs, M. Chaker, and B. J. Siwick, Science **346**, 445 (2014).
[26] M. Nakano, K. Shibuya, D. Okuyama, T. Hatano, S. Ono, M. Kawasaki, Y. Iwasa, and Y. Tokura, Nature (London) **487**, 459 (2012).
[27] E. Strelcov, A. Tselev, I. Ivanov, J. D. Budai, J. Zhang, J. Z. Tischler, I. Kravchenko, S. V. Kalinin, and A. Kolmakov, Nano Lett. **12**, 6198 (2012).
[28] H. Takami, T. Kanki, S. Ueda, K. Kobayashi, and H. Tanaka, Phys. Rev. B **85**, 205111 (2012).
[29] J. Sakai and M. Kurisu, Phys. Rev. B **78**, 033106 (2008).
[30] A. B. Pevtsov, A. V. Medvedev, D. A. Kurdyukov, N. D. Il'inskaya, V. G. Golubev, and V. G. Karpov, Phys. Rev. B **85**, 024110 (2012).
[31] K. Martens, J. W. Jeong, N. Aetukuri, C. Rettner, N. Shukla, E. Freeman, D. N. Esfahani, F. M. Peeters, T. Topuria, P. M. Rice *et al.*, Phys. Rev. Lett. **115**, 196401 (2015).
[32] C. Kübler, H. Ehrke, R. Huber, R. Lopez, A. Halabica, R. F. Haglund, and A. Leitenstorfer, Phys. Rev. Lett. **99**, 116401 (2007).
[33] D. I. Khomskii and T. Mizokawa, Phys. Rev. Lett. **94**, 156402 (2005).
[34] S. Wall, D. Wegkamp, L. Foglia, K. Appavoo, J. Nag, R. F. Haglund, Jr., J. Stahler, and M. Wolf, Nat. Commun. **3**, 721 (2012).
[35] C. Weber, D. D. O'Regan, N. D. M. Hine, M. C. Payne, G. Kotliar, and P. B. Littlewood, Phys. Rev. Lett. **108**, 256402 (2012).
[36] E. Morosan, D. Natelson, A. H. Nevidomskyy, and Q. Si, Adv. Mater. **24**, 4896 (2012).
[37] J. Laverock, S. Kittiwatanakul, A. A. Zakharov, Y. R. Niu, B. Chen, S. A. Wolf, J. W. Lu, and K. E. Smith, Phys. Rev. Lett. **113**, 216402 (2014).
[38] D. Wegkamp *et al.*, Phys. Rev. Lett. **113**, 216401 (2014).
[39] T. L. Cocker, L. V. Titova, S. Fourmaux, G. Holloway, H. C. Bandulet, D. Brassard, J. C. Kieffer, M. A. El Khakani, and F. A. Hegmann, Phys. Rev. B **85**, 155120 (2012).
[40] L. Bai, Q. Li, S. A. Corr, Y. Meng, C. Park, S. V. Sinogeikin, C. Ko, J. Wu, and G. Shen, Phys. Rev. B **91**, 104110 (2015).
[41] E. Arcangeletti, L. Baldassarre, D. Di Castro, S. Lupi, L. Malavasi, C. Marini, A. Perucchi, and P. Postorino, Phys. Rev. Lett. **98**, 196406 (2007).
[42] A. P. Peter *et al.*, Adv. Funct. Mater. **25**, 679 (2015).

[43] J. Jeong, N. Aetukuri, T. Graf, T. D. Schladt, M. G. Samant, and S. S. Parkin, Science **339**, 1402 (2013).
[44] A. Frenzel, M. M. Qazilbash, M. Brehm, B.-G. Chae, B.-J. Kim, H.-T. Kim, A. V. Balatsky, F. Keilmann, and D. N. Basov, Phys. Rev. B **80**, 115115 (2009).
[45] B. T. O'Callahan, A. C. Jones, J. Hyung Park, D. H. Cobden, J. M. Atkin, and M. B. Raschke, Nat. Commun. **6**, 6849 (2015).
[46] E. Dagotto, Science **309**, 257 (2005).
[47] See Supplemental Material at http://link.aps.org/supplemental/10.1103/PhysRevB.95.075433 for synchrotron radiation XRD for thickness of VO_2 thin films (Figs. S1); the evidence of the nanoscale domains (distorted M1) inlaying in the VO_2 (mM) matrix by near-field microwave microscopy (Figs. S2); the volume ratio of the mM and M1 phase in the VO_2 thin films is $\sim$1/3 by fitting the θ-2θ scans of the synchrotron radiation XRD and AFM (Figs. S3); the microscopic images by conductive atomic force microscopy (Figs. S4); synchrotron radiation reciprocal space mapping at *in situ* varying temperatures for mixed-phase VO_2 thin films, indicating that the monoclinic structure has been clamped across the MIT by the substrates (Figs. S5); Raman active modes of the VO_2 through theoretical calculations, and some details about the UPS characterizations (Figs. S6, S8); XRD spectra of the pure VO_2 (M1) and pure VO_2 (R) films deposited onto sapphire substrates with (0001)-orientation (Figs. S7).
[48] M. M. Qazilbash *et al.*, Science **318**, 1750 (2007).
[49] J. Burgy, M. Mayr, V. Martin-Mayor, A. Moreo, and E. Dagotto, Phys. Rev. Lett. **87**, 277202 (2001).
[50] B. Gjonaj, A. David, Y. Blau, G. Spektor, M. Orenstein, S. Dolev, and G. Bartal, Nano Lett. **14**, 5598 (2014).
[51] A. C. Jones, S. Berweger, J. Wei, D. Cobden, and M. B. Raschke, Nano Lett. **10**, 1574 (2010).
[52] Y. G. Jeong *et al.*, Nano Lett. **15**, 6318 (2015).
[53] H. Ji, J. Wei, and D. Natelson, Nano Lett. **12**, 2988 (2012).
[54] Julie Karel *et al.*, ACS Nano **8**, 5784 (2014).
[55] M. Yang *et al.*, RSC Adv. **5**, 80122 (2015).
[56] J. Lu, K. G. West, and S. A. Wolf, Appl. Phys. Lett. **93**, 262107 (2008).
[57] M. Yang *et al.*, Sci. Rep. **6**, 23119 (2016).
[58] H. T. Zhang, L. Zhang, D. Mukherjee, Y. X. Zheng, R. C. Haislmaier, N. Alem, and R. Engel-Herbert, Nat. Commun. **6**, 8475 (2015).
[59] M. C. Biesinger, L. W. M. Lau, A. R. Gerson, and R. S. C. Smart, Appl. Surf. Sci. **257**, 887 (2010).
[60] C. Marini *et al.*, Phys. Rev. B **77**, 235111 (2008).
[61] S. J. Chang *et al.*, Nanoscale **6**, 8068 (2014).
[62] C. H. Chen, Y. H. Zhu, Y. Zhao, J. H. Lee, H. Y. Wang, A. Bernussi, M. Holtz, and Z. Y. Fan, Appl. Phys. Lett. **97**, 211905 (2010).
[63] L. L. Fan, Y. F. Wu, C. Si, G. Q. Pan, C. W. Zou, and Z. Y. Wu, Appl. Phys. Lett. **102**, 011604 (2013).
[64] T. C. Koethe *et al.*, Phys. Rev. Lett. **97**, 116402 (2006).
[65] J. B. Goodenough, J. Solid State Chem. **3**, 490 (1971).
[66] R. Hillenbrand, T. Taubner, and F. Keilmann, Nature (London) **418**, 159 (2002).
[67] F. Keilmann and R. Hillenbrand, Philos. Trans. R. Soc. London, Ser. A **362**, 787 (2004).